Electronic Supplementary Material (ESI) for Environmental Science: Nano.

Supplementary material for:

Few-layer graphitic carbon nitride for enhanced visible-light photocatalytic efficiency: the role of narrow bandgap and nitrogen-vacancies

Qiang Huang, Yang Liu, Wenhui Bai, Jiahui Hong, Yuejie Ai* and Zhe Chen*

MOE Key Lab of Resources and Environmental System optimization, College of Environmental Science and Engineering, North China Electric Power University, Beijing 102206, P. R. China

Corresponding authors. Email: chenz@ncepu.edu.cn

Content

Text S1 HPLC analysis conditions

BPA: The samples were filtered with 0.22 μm polyethersulfone syringe membrane filter to determine the BPA concentration via HPLC (Agilent 1260 Infinity Ⅱ, USA) with an Agilent InfinityLab Poroshell 120 EC-C18 column (4.6 × 150 mm, 4 μm). The mobile phase was a mixture of 70% methanol and 30% water. The flow rate and injection volumes were 0.5 mL/min and 10 μL, respectively. The detector wavelength was set at 225 nm. The retention time of BPA was 5.7 min.

Phenol: The samples were filtered with 0.22 μm polyethersulfone syringe membrane filter to determine the phenol concentration via HPLC (Agilent 1260 Infinity Ⅱ, USA) with an Agilent InfinityLab Poroshell 120 EC-C18 column (4.6 × 150 mm, 4 μm). The mobile phase was a mixture of 60% methanol and 40% water. The flow rate and injection volumes were 0.5 mL/min and 20 μL, respectively. The detector wavelength was set at 275 nm. The retention time of phenol was 4.8 min.

4-CP: The samples were filtered with 0.22 μm polyethersulfone syringe membrane filter to determine the 4-CP concentration via HPLC (Agilent 1260 Infinity Ⅱ, USA) with an Agilent InfinityLab Poroshell 120 EC-C18 column (4.6 × 150 mm, 4 μm). The mobile phase was a mixture of 70% methanol and 30% water. The flow rate and injection volumes were 0.5 mL/min and 10 μL, respectively. The detector wavelength was set at 280 nm. The retention time of 4-CP was 5.2 min.

2,4-DCP: The samples were filtered with 0.22 μm polyethersulfone syringe membrane filter to determine the 2,4-DCP concentration via HPLC (Agilent 1260 Infinity Ⅱ, USA) with an Agilent InfinityLab Poroshell 120 EC-C18 column (4.6 × 150 mm, 4 μm). The mobile phase was a mixture of 70% methanol and 30% water. The flow rate and injection volumes were 0.5 mL/min and 10 μL, respectively. The detector wavelength was set at 220 nm. The retention time of 2,4-DCP was 7.2 min.

2,4,6-TCP: The samples were filtered with 0.22 μm polyethersulfone syringe membrane filter to determine the 2,4,6-TCP concentration via HPLC (Agilent 1260 Infinity Ⅱ, USA) with an Agilent InfinityLab Poroshell 120 EC-C18 column (4.6 × 150 mm, 4 μm). The mobile phase was a mixture of 80% methanol and 20% water.

The flow rate and injection volumes were 1.0 mL/min and 20 μL, respectively. The detector wavelength was set at 290 nm. The retention time of 2,4,6-TCP was 3.4 min.

TC: The samples were filtered with 0.22 μm polyethersulfone syringe membrane filter to determine the TC concentration via HPLC (Agilent 1260 Infinity Ⅱ, USA) with an Agilent InfinityLab Poroshell 120 EC-C18 column (4.6 × 150 mm, 4 μm). The mobile phase was a mixture of 20% acetonitrile and 80% water with 0.1% formic acid. The flow rate and injection volumes were 1.0 mL/min and 20 μL, respectively. The detector wavelength was set at 280 nm. The retention time of TC was 3.4 min.

Text S2 Density functional theory (DFT) calculation

In this section, theoretical calculations were further carried out to investigate the influence of thickness and nitrogen-vacancy (NV) of g-C_3N_4 on the electronic characteristics by the spin-polarized density functional theory (DFT) method implemented in the Vienna ab-initio simulation package (VASP) [1]. The g-C_3N_4 model was constructed based on the crystal structure with lattice parameters of a=b=7.38 Å, α=β=90°, γ=120° (see **Fig. S10A**) [2]. As shown in **Fig. S10B**, a 2×2×1 supercell was then built up based on the unit cell, while monolayer and four layers of g-C_3N_4 were selected as the computational models of thin and thick g-C_3N_4 materials, respectively. A 15 Å vacuum was added in the Z direction to avoid the periodicity-induced effect. The exchange-correlation functional of Perdew-Burke-Ernzerhof (PBE) within Generalized Gradient Approximation (GGA) was employed to describe the exchange-correlation energy [3], and the energy cut-off was set at 500 eV. Moreover, the D3 vdW correction proposed by S. Grimme was also employed in considering the dispersive interaction in the calculation process [4, 5]. All the atoms were fully relaxed when the Hellmann-Feynman force was less than 0.01 eV/Å, and the energy convergence criteria was set to 10^{-5} eV. For geometric optimization, the Brillouin-zone integrations were sampled with the 3 × 3 × 1 k-point set of Monkhorst-Pack scheme. For the

density of state (DOS) calculations, Brillouin-zone integrations were performed using the G-centered 7 × 7 × 1 k mesh.

Text S3 Results and discussion

Text S3.1 XRD spectrum analysis

The X-ray powder diffractometer (XRD) pattern (**Fig. 2B** in the main text) of B-C_3N_4 had two strong peaks at 27.4° and 13.3°, corresponding to the (002) and (100) crystal planes, respectively. As for the few-layer g-C_3N_4 nanosheet, the peak (002) decreased, while the peak (100) almost disappeared, indicating the poor condensation degree and reduced dimension structure [6]. A new peak at 18.5° was observed from the XRD pattern of the few-layer g-C_3N_4 nanosheet, indexed to the plane (310) of heptazine-based g-C_3N_4 [7]. The appearance of the strong peak (310) indicated the basic units of the few-layer g-C_3N_4 nanosheet were heptazine (tri-s-triazine).

Text S3.2 FT-IR spectrum analysis

The FT-IR spectrum (**Fig. S8A**) for B-C_3N_4 showed several peaks at 3000-3500 cm^{-1}, 1200-1700 cm^{-1}, and 808 cm^{-1}, corresponding to N-H/O-H, CN heterocycles stretching vibrations, and characteristic breathing mode of tri-s-triazine, respectively [8]. Compared to the B-C_3N_4, a new peak at 2175 cm^{-1} appeared on the Fourier transform infrared (FT-IR) spectrum of few-layer g-C_3N_4 nanosheet (**Fig. S8B**), corresponding to the asymmetric vibration of -C≡N [9]. The presence of the -C≡N group was attributed to the nitrogen loss from the tri-s-triazine heterocycles open process, revealing the existence of NVs in the few-layer g-C_3N_4 nanosheet [9].

Text S3.3 DFT analysis

The theoretical calculation was taken to investigate the influence of thickness and NV of g-C_3N_4 on the electronic characteristics. The optimized monolayer and multilayer structures of pure g-C_3N_4 were shown in **Fig. S11A**. In general, the bond

distance of C-N was 1.35 Å and the ∠NCN angle were 123.51° and 123.29° for mono- and multilayer g-C_3N_4, respectively. The density of states (DOS) plots for mono- and multilayer g-C_3N_4 were presented in **Fig. 5A** and **Fig. 5B**, respectively. It could be observed that the VB edge of the monolayer was mainly contributed by N 2p orbital, and the CB edge was composed of C 2p and N 2p orbitals, which was consistent with previous studies [10]. Whereas, for the multilayer pure g-C_3N_4 system, both VB and CB edges were occupied by C 2p and N 2p orbitals. In addition, the calculated bandgap of monolayer g-C_3N_4 (1.47 eV) was much narrower than the multilayer system (1.54 eV), which was more conducive to the visible-light absorption.

The influence of NV on the configuration and electronic characteristics of g-C_3N_4 was also taken into consideration. As seen in **Fig. S10C**, three kinds of nonequivalent N atoms (noted as N1, N2, and N3) in a heptazine unit were proposed to be the possible sites of NV. Based on this, three kinds of NV systems for g-C_3N_4 (abbreviated as g-C_3N_4@NV) were constructed for both mono- and multilayer systems. The formation energies of g-C_3N_4@NV were calculated as follows:

$$E_f = E(g\text{-}C_3N_4@NV)\text{-}[E(g\text{-}C_3N_4)\text{-}\mu(N)] \quad (1)$$

Where $E(g\text{-}C_3N_4@NV)$ and $E(g\text{-}C_3N_4)$ represented the total energies of g-C_3N_4@NV and g-C_3N_4, respectively, and the $\mu(N)$ denoted the chemical potential of single N atom.

The optimized structures and mono- and multilayer g-C_3N_4@NV systems were depicted in **Fig. S11B** and **Fig. S11C**, respectively, and the corresponding formation energies were summarized in **Table S3**. It could be noticed that the formation energies of N3 vacancy on the mono- and multilayer g-C_3N_4 were 2.69 and 2.91 eV, respectively, which were much more negative than the corresponding N1 and N2

vacancies. This meant that the N3 vacancy systems were more favorable from the perspective of formation energies, which was consistent with the XPS analysis. Thus, the subsequent discussions were based on these two configurations. Firstly, it could be observed from **Fig. S11B** and **Fig. S11C**_that the C-N bond lengths of the heptazine containing NV decreased (1.27 Å in monolayer g-C_3N_4@NV and 1.23 Å in multilayer g-C_3N_4@NV) compared with the corresponding pure g-C_3N_4 systems. And the ∠NCN bond angles were reduced to 119.66° and 116.85° for mono- and multilayer g-C_3N_4@NV, respectively. These configurations suggested that the incorporation of NV induced partial distortion of triazine ring for both mono- and multilayer g-C_3N_4, which was beneficial for the separation of charge-carriers [11]. The density of states of mono- and multilayer g-C_3N_4@NV were investigated in **Fig. 5C** and **Fig. 5D.** The bandgap of monolayer g-C_3N_4@NV narrowed to 0.57 eV after the introduction of NV. Besides, it was worth mentioning that the incorporation of NV into monolayer g-C_3N_4@NV introduced additional mid-gap state at the bottom of the CB (labeled in black dotted line), which was mainly contributed by C 2p and N 2p orbitals. There was also a distinct reorganization of bands due to the existence of NV in the vicinity of the Fermi level (between -1 and 0.5 eV for monolayer g-C_3N_4@NV, between -1.5 and -1 eV for multilayer g-C_3N_4@NV) in the PDOS plots [12]. These results were got corroborated mutually in UV-vis DRS analysis showing that the introduction of NV led to a lowering of bandgap energy.

Text S3.4 Analysis of possible degradation pathway toward 2,4,6-TCP

To understand the photocatalytic degradation of chlorophenol pollutants by the few-layer g-C_3N_4 nanosheet, the intermediate samples from the photocatalysis degradation of 2,4,6-TCP were detected using HPLC-MS spectra (Ultimate 3000 UHPLC-Q Exactive HPLC-MS). As shown in **Fig. S13A**, before the photocatalysis,

only one sample was detected at 8.47 min, which was assigned to 2,4,6-TCP itself (**Fig. S13B**). After reaction for 1 h, two types of possible intermediate samples were found at 4.10 min and 2.44 min, respectively. According to the mass-to-charge ratios (m/z) analysis and previous reports [13], the intermediate samples at 4.10 min and 2.44 min were assigned to 2,6-dichlorohydroquinone (2,6-DCHQ) (**Fig. S13C**) and 2,6-dichloro-3-hydroxy-1,4-benzoquinone (2,6-DCHB) (**Fig. S13D**), respectively. After 24 h of continuous photocatalytic degradation, only the 2,6-DCHB could be detected. Based on the discussion above, the possible degradation pathway of 2,4,6-TCP by the few-layer g-C_3N_4 nanosheet was shown in **Fig. S13E**. In the degradation process of 2,4,6-TCP over the few-layer g-C_3N_4 nanosheet, the 2,4,6-TCP was firstly destructed by $\bullet O_2^-$/ h^+/$^1O_2$ species through a dechlorination process and oxidized to be 2,6-DCHQ, followed by a hydroxylation process to be 2,6-DCHB. By this degradation path, the 2,4,6-TCP was oxidized and mineralized by step to environment-friendly small-molecular compounds, CO_2 and H_2O [14].

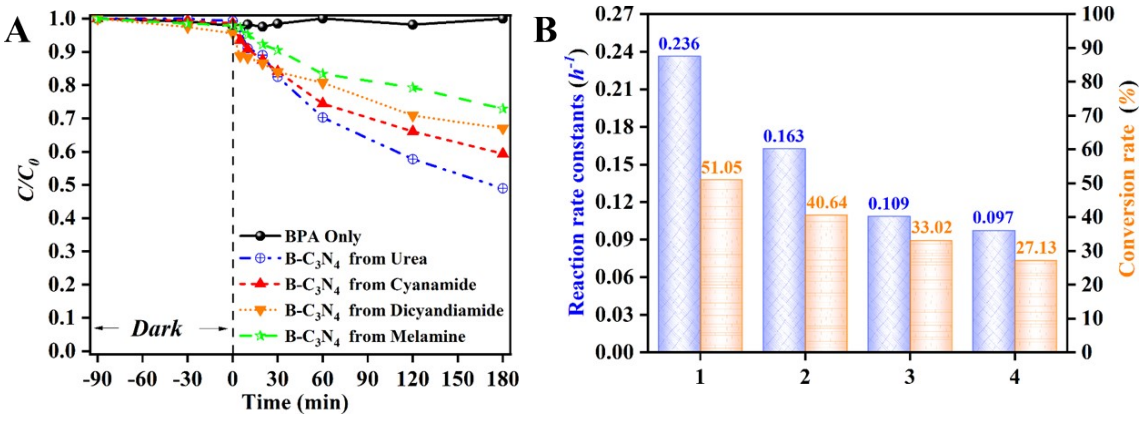

Fig. S1 (A) Photocatalytic activities for the degradation of BPA over different B-C_3N_4 materials (C_{BPA} = 10 mg L^{-1}, Dosage = 20 mg, Volume = 50 mL, T = 298.15 K, 380 nm ≤ λ ≤ 780 nm); (B) Reaction rate constants according to the first-order kinetics and corresponding conversion rates (the samples 1, 2, 3, 4 refer to the B-C_3N_4 derived from urea, cyanamide, dicyandiamide, and melamine, respectively).

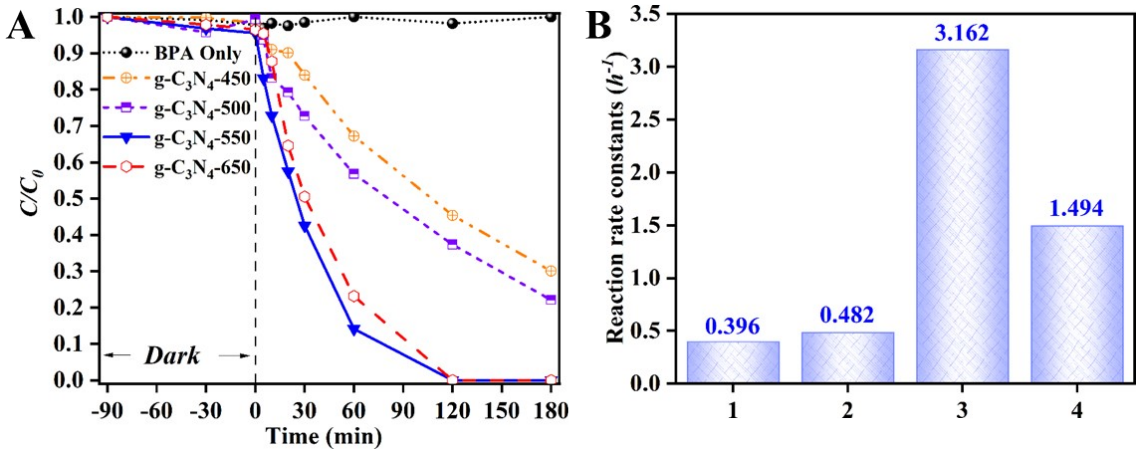

Fig. S2 (A) Photocatalytic activities for the degradation of BPA over different few-layer g-C_3N_4 nanosheets (C_{BPA} = 10 mg L^{-1}, Dosage = 20 mg, Volume = 50 mL, T = 298.15 K, 380 nm ≤ λ ≤ 780 nm); (B) Reaction rate constants according to the first-order kinetics (the samples 1, 2, 3, 4 refer to the few-layer g-C_3N_4 nanosheets prepared at 450, 500, 550, 650 ºC, respectively).

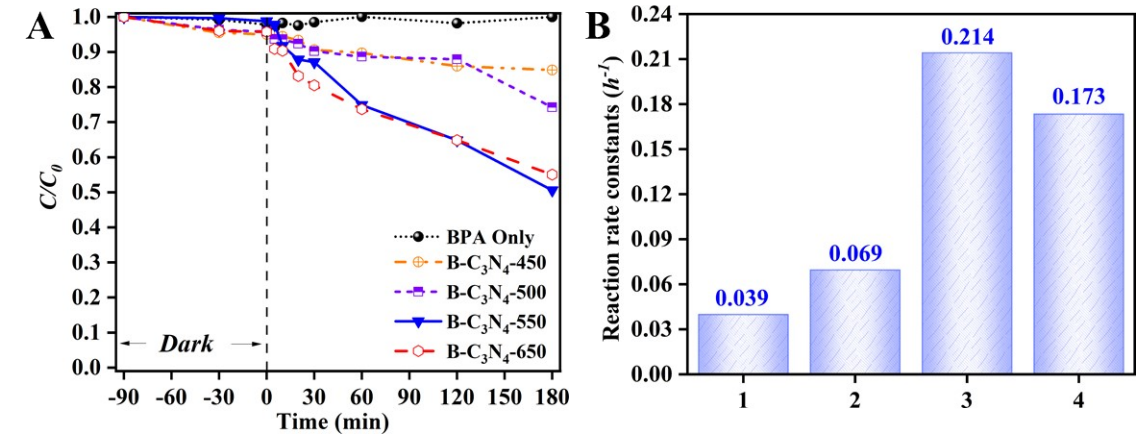

Fig. S3 (A) Photocatalytic activities for the degradation of BPA over different B-C_3N_4 materials (C_{BPA} = 10 mg L^{-1}, Dosage = 20 mg, Volume = 50 mL, T = 298.15 K, 380 nm ≤ λ ≤ 780 nm); (B) Reaction rate constants according to the first-order kinetics in 180 min (the samples 1, 2, 3, 4 refer to the B-C_3N_4 prepared at 450, 500, 550, 650 ºC, respectively).

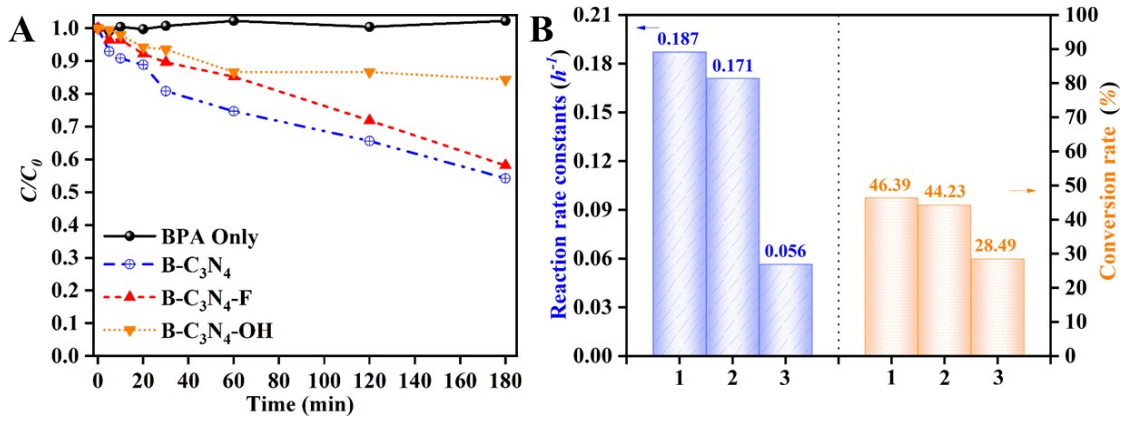

Fig. S4 (A) Photocatalytic activities for the degradation of BPA over different B-C_3N_4 materials (C_{BPA} = 10 mg L^{-1}, Dosage = 20 mg, Volume = 50 mL, T = 298.15 K, 380 nm ≤ λ ≤ 780 nm); (B) Reaction rate constants according to the first-order kinetics and corresponding conversion rates in 180 min (the samples 1, 2, 3 refer to the B-C_3N_4, B-C_3N_4-F, B-C_3N_4-OH, respectively).

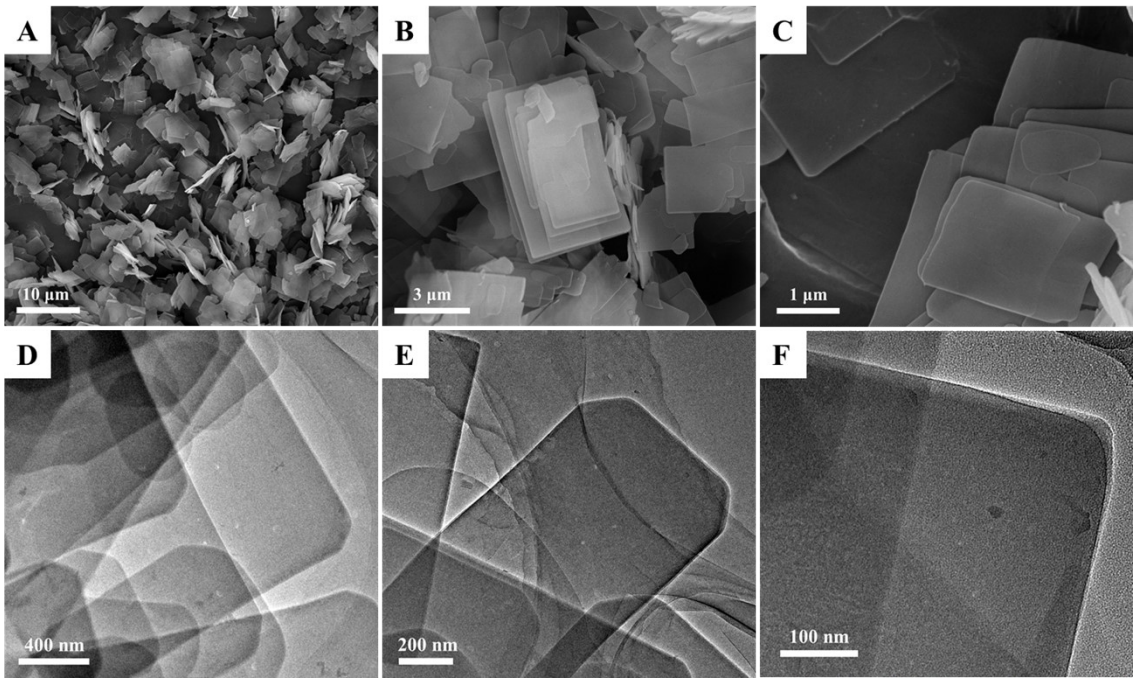

Fig. S5 (A-C) SEM images and (D-F) TEM images of the template RUB-15.

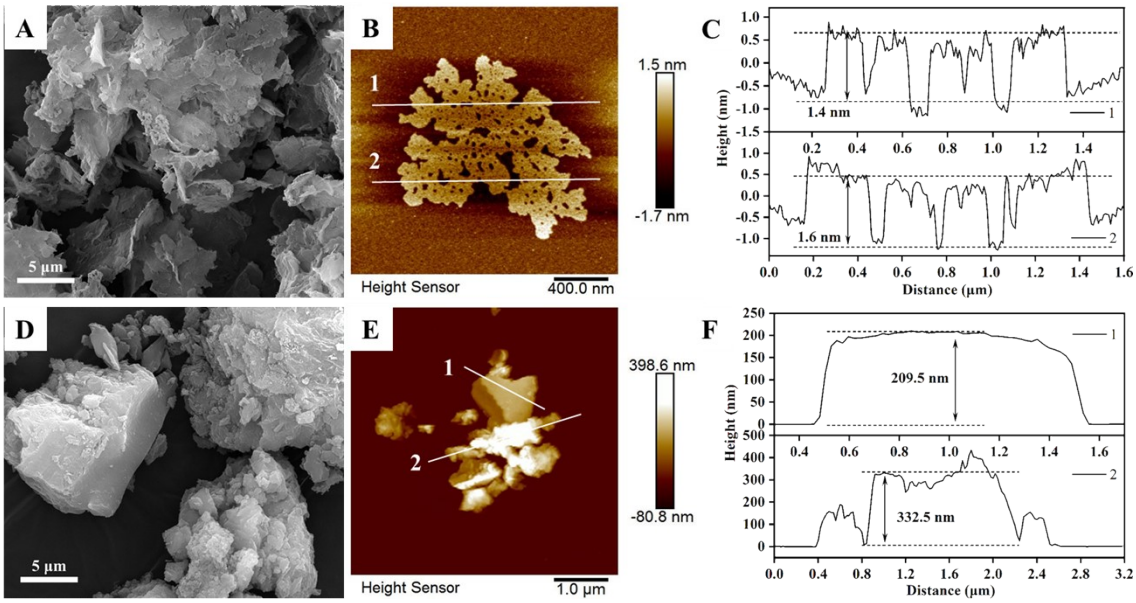

Fig. S6 (A) SEM image, (B) AFM image, and (C) corresponding thickness analysis taken around the white line in (B) of few-layer g-C_3N_4 nanosheet; (D) SEM image, (E) AFM image, and (F) corresponding thickness analysis taken around the white line in (F) of B-C_3N_4.

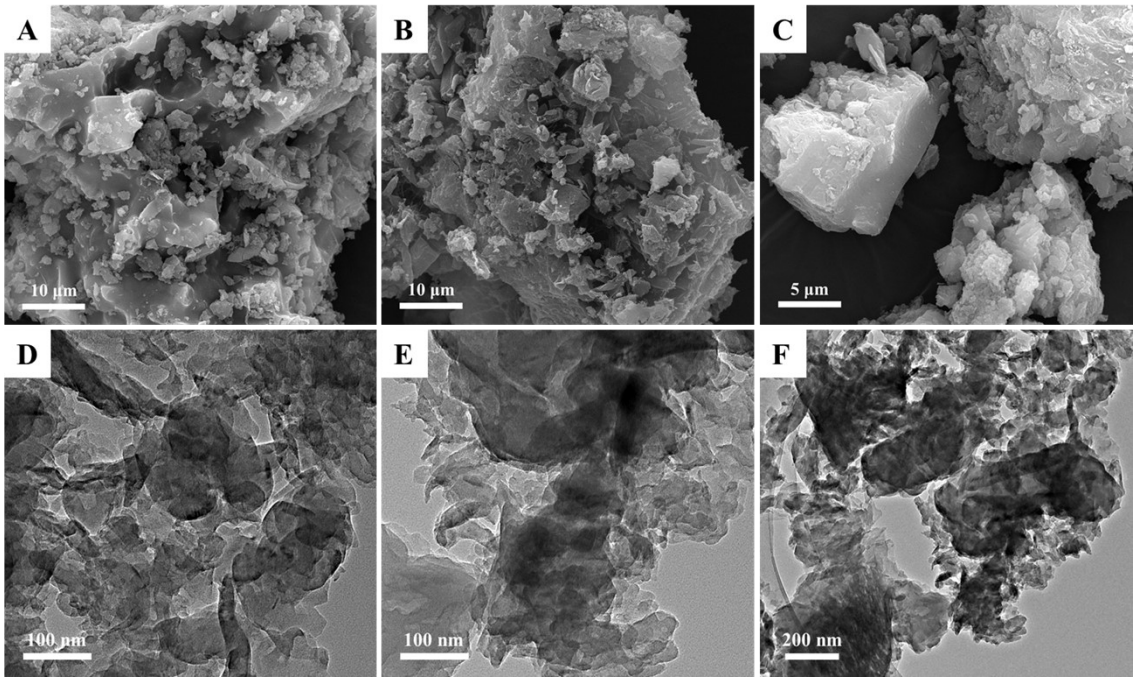

Fig. S7 (A-C) SEM images and (D-F) TEM images of B-C_3N_4.

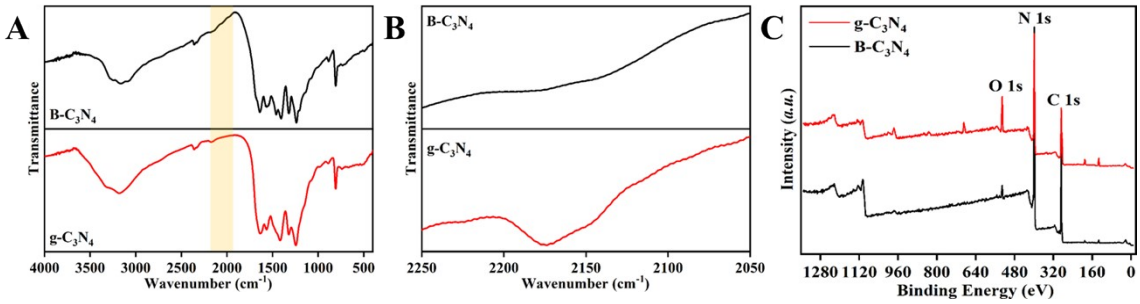

Fig. S8 (A) FT-IR spectra, (C) enlarged view of FT-IR, and (C) XPS survey spectra of B-C_3N_4 and few-layer g-C_3N_4 nanosheet.

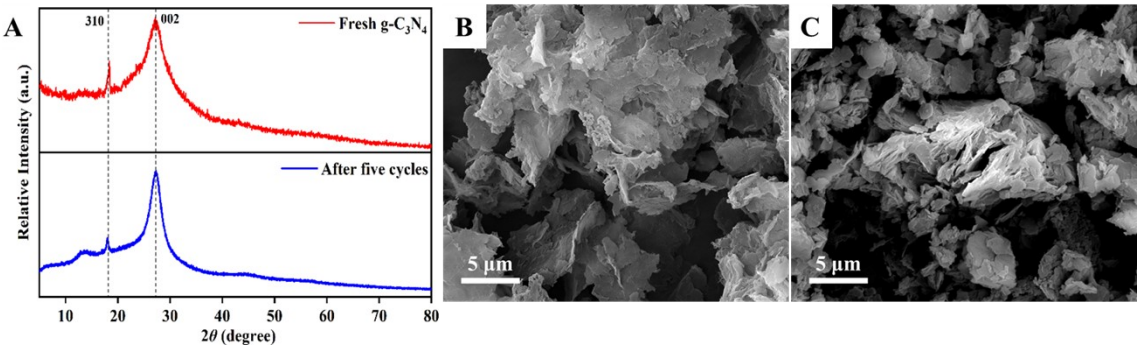

Fig. S9 (A) XRD spectra of the fresh g-C_3N_4 nanosheet and the product after five catalysis cycles; SEM images of the few-layer g-C_3N_4 nanosheet (B) before and (C) after being used for five cycles.

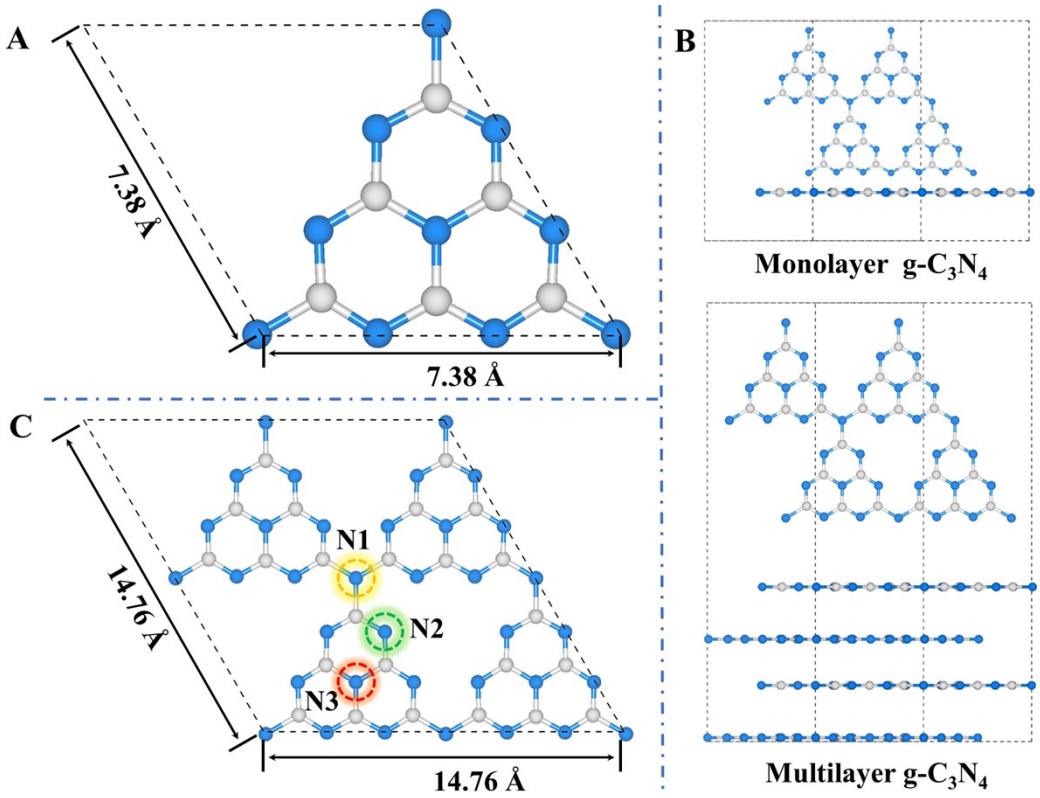

Fig. S10 (A) Lattice parameters for the unit cell; (B) Geometric models for monolayer and multilayer g-C_3N_4; (C) The non-equivalent sites of NV (The C and N atoms were shown as grey and blue spheres, respectively.).

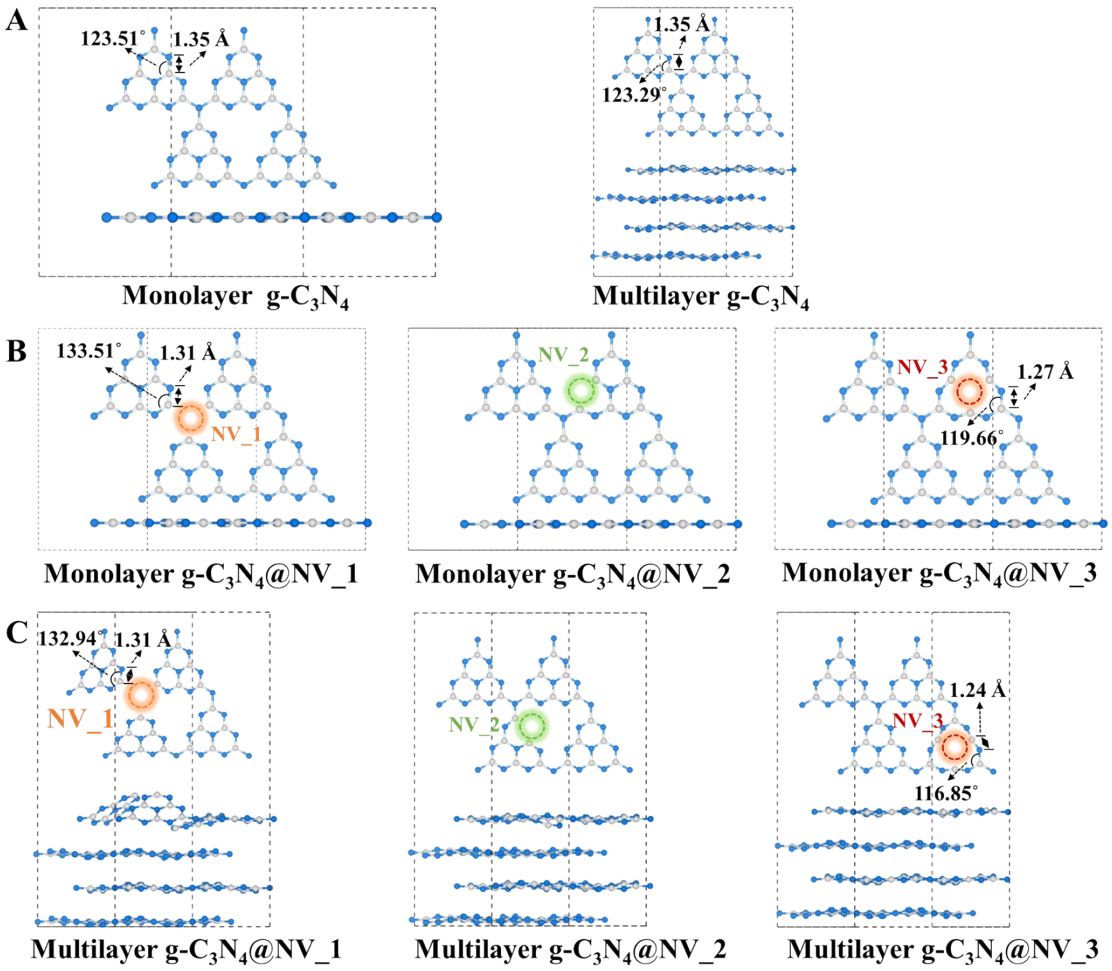

Fig. S11 Optimized structures of (A) monolayer and multilayer g-C_3N_4 without nitrogen vacancy, (B) monolayer g-C_3N_4@NV, and (C) multilayer g-C_3N_4@NV.

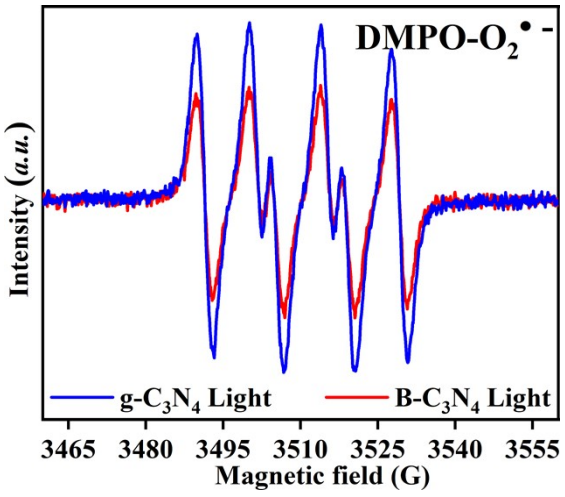

Fig. S12 EPR spectra of DMPO-•O_2^- from few-layer g-C_3N_4 nanosheet and B-C_3N_4.

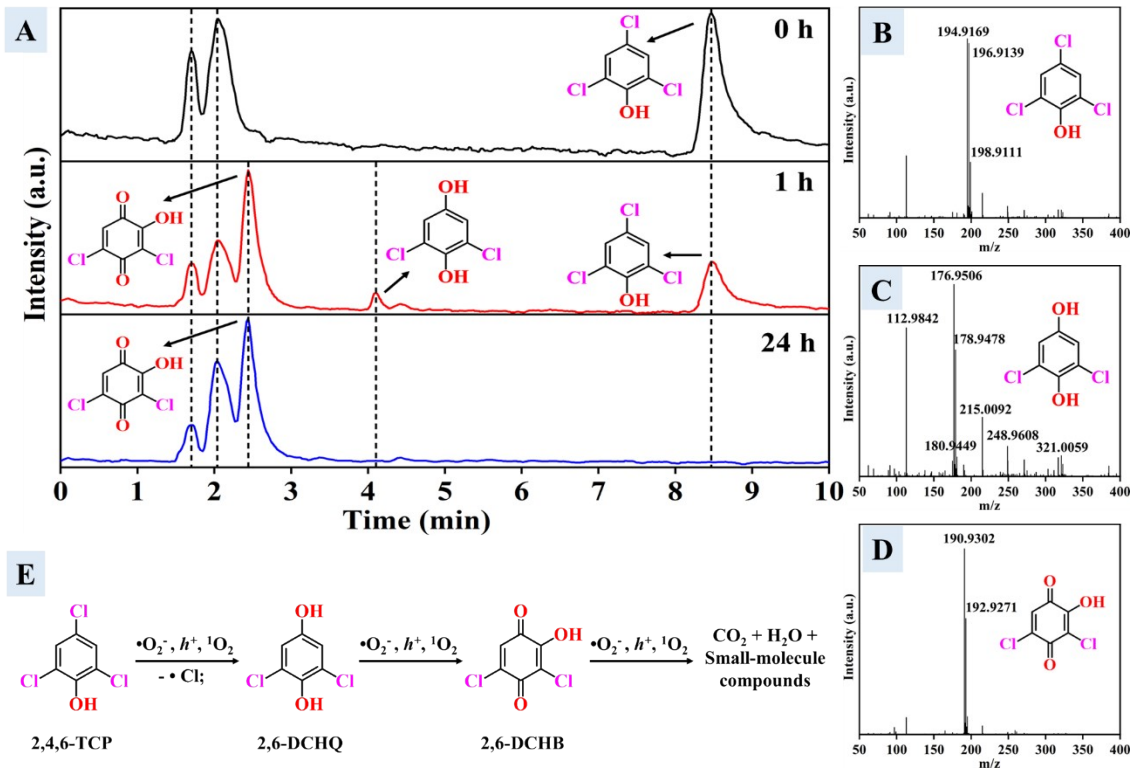

Fig. S13 (A) HPLC-MS chromatograms of the intermediate sample from the photocatalysis degradation of 2,4,6-TCP; The mass spectra of (B) 2,4,6-TCP, (C) 2,6-DCHQ, and (D) 2,6-DCHB; (E) Flow diagram of 2,4,6-TCP degradation pathway.

Table S1 BET surface areas of B-C_3N_4 and few-layer g-C_3N_4 nanosheet.

Samples	**BET surface area (m^2 g^{-1})**
B-C_3N_4	19.66
Few-layer g-C_3N_4 nanosheet	40.65

Table S2 Element content and atomic ratio of B-C_3N_4 and few-layer g-C_3N_4 nanosheet.

Samples	**C** (%)	**N** (%)	**O** (%)	**O/C**	**N/C**
B-C_3N_4	40.23	57.02	2.48	0.06	1.42
Few-layer g-C_3N_4 nanosheet	42.24	45.73	9.11	0.22	1.08

Table S3 The calculated formation energies of monolayer and multilayer g-C_3N_4@ NV.

Model	**Site**	**Formation energies/eV**
Monolayer g-C_3N_4	Site 1	5.02
	Site 2	3.31
	Site 3	2.69
Multilayer g-C_3N_4	Site 1	3.95
	Site 2	3.28
	Site 3	2.91

Table S4 Comparative study of the photocatalytic performance of other C_3N_4-based photocatalysts under similar conditions.

Photocatalysts	Organic contaminants	Reaction rate (h^{-1})	Experimental conditions			Ref
			T (°C)	Dosage (g L^{-1})	C_0 (mg L^{-1})	
UWCN	BPA	2.502	25	0.2	20	[15]
CeO_2/CNNS-3	BPA	2.004	25	1.0	10	[16]
Carbon-defect-modified g-C_3N_4	BPA	0.336	25	0.3	10	[17]
Few-layer g-C_3N_4 nanosheet	**BPA**	**3.162**	**25**	**0.4**	**10**	**This work**
Phosphorus- and Sulfur-Codoped g-C_3N_4	TC	2.293	-	1.0	10	[18]
h-BN/g-C_3N_4 heterojunction	TC	1.665	-	1.0	10	[19]
S-CQDs/hollow tubular g-C_3N_4	TC	1.758	-	1.0	20	[20]
Few-layer g-C_3N_4 nanosheet	**TC**	**4.629**	**25**	**0.4**	**10**	**This work**
CdS(10 wt%)/g-C_3N_4	4-CP	0.064	-	1.0	20	[21]
ZnO/g-C_3N_4	4-CP	0.186	25	0.2	10	[22]
Few-layer g-C_3N_4 nanosheet	**4-CP**	**0.158**	25	0.4	10	This work

Ag_2CrO_4/Ag/g-C_3N_4	2,4-DCP	0.910	-	1.0	10	[23]
Few-layer g-C_3N_4 nanosheet	**2,4-DCP**	**0.347**	**25**	**0.4**	**10**	**This work**
$BiOIO_3$/g-C_3N_4-30 wt%	2,4,6-TCP	0.970	-	-	50	[24]
Few-layer g-C_3N_4 nanosheet	**2,4,6-TCP**	**0.352**	**25**	**0.4**	**10**	**This work**
$LaCoO_3$/g-C_3N_4-20 wt%	Phenol	0.100	25	1.0	20	[25]
$LaCoO_3$/g-C_3N_4-30 wt%	Phenol	0.050	-	1.0	20	[25]
$LaCoO_3$/g-C_3N_4-40 wt%	Phenol	0.150	-	1.0	20	[25]
$LaCoO_3$/g-C_3N_4-50 wt%	Phenol	0.060	-	1.0	20	[25]
$LaCoO_3$/g-C_3N_4-60 wt%	Phenol	0.390	-	1.0	20	[25]
$LaCoO_3$/g-C_3N_4-70 wt%	Phenol	0.230	-	1.0	20	[25]
Few-layer g-C_3N_4 nanosheet	**Phenol**	**0.208**	**25**	**0.4**	**10**	**This work**

References

1. G. Kresse and D. Joubert, From ultrasoft pseudopotentials to the projector augmented-wave method, *Phys. Rev. B*, 1999, **59**, 1758-1775.
2. C. L. Zhang, Y. Liu, X. Li, H. X. Chen, T. Wen, Z. H. Jiang, Y. J. Ai, Y. B. Sun, T. Hayat and X. K. Wang, Highly uranium elimination by crab shells-derived porous graphitic carbon nitride: Batch, EXAFS and theoretical calculations, *Chem. Eng. J.*, 2018, **346**, 406-415.
3. J. P. Perdew, K. Burke and M. Ernzerhof, Generalized Gradient Approximation Made Simple, *Phys. Rev. Lett.*, 1996, **77**, 3865-3868.
4. S. Grimme, J. Antony, S. Ehrlich and H. Krieg, A consistent and accurate ab initio parametrization of density functional dispersion correction (DFT-D) for the 94 elements H-Pu, *J. Chem. Phys.*, 2010, **132**, 154104.
5. S. Grimme, S. Ehrlich and L. Goerigk, Effect of the damping function in dispersion corrected density functional theory, *J. Comput. Chem.*, 2011, **32**, 1456-1465.
6. F. Guo, B. Hu, C. Yang, J. Zhang, Y. Hou and X. Wang, On-Surface Polymerization of In-Plane Highly Ordered Carbon Nitride Nanosheets toward Photocatalytic Mineralization of Mercaptan Gas, *Adv. Mater.*, 2021, **33**, 2101466.
7. Q. Dong, N. Mohamad Latiff, V. Mazánek, N. F. Rosli, H. L. Chia, Z. Sofer and M. Pumera, Triazine- and Heptazine-Based Carbon Nitrides: Toxicity, *ACS Appl. Nano Mater.*, 2018, **1**, 4442-4449.
8. R. Dadigala, R. Bandi, B. R. Gangapuram and V. Guttena, Carbon dots and Ag nanoparticles decorated g-C_3N_4 nanosheets for enhanced organic pollutants degradation under sunlight irradiation, *J. Photochem. Photobiol., A*, 2017, **342**, 42-52.
9. H. Yu, R. Shi, Y. Zhao, T. Bian, Y. Zhao, C. Zhou, G. I. N. Waterhouse, L.-Z. Wu, C.-H. Tung and T. Zhang, Alkali-Assisted Synthesis of Nitrogen Deficient Graphitic Carbon Nitride with Tunable Band Structures for Efficient Visible-Light-Driven Hydrogen Evolution, *Adv. Mater.*, 2017, **29**, 1605148.
10. B. Zhu, L. Zhang, B. Cheng and J. Yu, First-principle calculation study of tri-s-triazine-based g-C_3N_4: A review, *Appl. Catal., B*, 2018, **224**, 983-999.
11. H. Wang, X. Zhang, J. Xie, J. Zhang, P. Ma, B. Pan and Y. Xie, Structural distortion in graphitic-C_3N_4 realizing an efficient photoreactivity, *Nanoscale*, 2015, **7**, 5152-5156.
12. J. Goclon and K. Winkler, Influence of nitrogen vacancies on selective oxidation of aromatic alcohols on g-C_3N_4: A comparative DFT study, *Mol. Catal.*, 2020, **482**, 110747.
13. H. Ji, F. Chang, X. Hu, W. Qin and J. Shen, Photocatalytic degradation of 2,4,6-trichlorophenol over g-C_3N_4 under visible light irradiation, *Chem. Eng. J.*, 2013, **218**, 183-190.
14. H. Wang, H. Guo, N. Zhang, Z. Chen, B. Hu and X. Wang, Enhanced Photoreduction of U(VI) on C_3N_4 by Cr(VI) and Bisphenol A: ESR, XPS, and EXAFS Investigation, *Environ. Sci. Technol.*, 2019, **53**, 6454-6461.
15. M. Zhang, Y. Yang, X. An, J. Zhao, Y. Bao and L.-a. Hou, Exfoliation method matters: The microstructure-dependent photoactivity of g-C_3N_4 nanosheets for water purification, *J. Hazard. Mater.*, 2022, **424**, 127424.
16. R. Ma, S. Zhang, L. Li, P. Gu, T. Wen, A. Khan, S. Li, B. Li, S. Wang and X. Wang, Enhanced Visible-Light-Induced Photoactivity of Type-II CeO_2/g-C_3N_4 Nanosheet toward Organic Pollutants Degradation, *ACS Sustainable Chem. Eng.*, 2019, **7**, 9699-9708.
17. X. Liang, G. Wang, X. Dong, G. Wang, H. Ma and X. Zhang, Graphitic Carbon Nitride with Carbon Vacancies for Photocatalytic Degradation of Bisphenol A, *ACS Appl. Nano Mater.*, 2019, **2**, 517-524.
18. L. Jiang, X. Yuan, G. Zeng, X. Chen, Z. Wu, J. Liang, J. Zhang, H. Wang and H. Wang, Phosphorus- and Sulfur-Codoped g-C_3N_4: Facile Preparation, Mechanism Insight, and Application as Efficient Photocatalyst for Tetracycline and Methyl Orange Degradation under Visible Light Irradiation, *ACS Sustainable Chem. Eng.*, 2017, **5**, 5831-5841.
19. L. Jiang, X. Yuan, G. Zeng, Z. Wu, J. Liang, X. Chen, L. Leng, H. Wang and H. Wang, Metal-free efficient photocatalyst for stable visible-light photocatalytic degradation of refractory pollutant, *Appl. Catal., B*, 2018, **221**, 715-725.
20. W. Wang, Z. Zeng, G. Zeng, C. Zhang, R. Xiao, C. Zhou, W. Xiong, Y. Yang, L. Lei, Y. Liu, D. Huang, M. Cheng, Y. Yang, Y. Fu, H. Luo and Y. Zhou, Sulfur doped carbon quantum dots loaded hollow tubular g-C_3N_4 as novel photocatalyst for destruction of Escherichia coli and tetracycline degradation under visible light, *Chem. Eng. J.*, 2019, **378**, 122132.

21. H. Shi, X. Jiang, Y. Li, D. Chen, C. Hou, Z. Zhang, Q. Zhang and J. Shen, Enhanced bio-photodegradation of p-chlorophenol by CdS/g-C_3N_4 3D semiconductor-microbe interfaces, *Sci. Total Environ.*, 2022, **807**, 151006.
22. J. G. M. de Sousa, T. V. C. da Silva, N. P. de Moraes, M. L. Caetano Pinto da Silva, R. da Silva Rocha, R. Landers and L. A. Rodrigues, Visible light-driven ZnO/g-C_3N_4/carbon xerogel ternary photocatalyst with enhanced activity for 4-chlorophenol degradation, *Mater. Chem. Phys.*, 2020, **256**, 123651.
23. Y. Gong, X. Quan, H. Yu and S. Chen, Synthesis of Z-scheme Ag_2CrO_4/Ag/g-C_3N_4 composite with enhanced visible-light photocatalytic activity for 2,4-dichlorophenol degradation, *Appl. Catal., B*, 2017, **219**, 439-449.
24. Y. Gong, X. Quan, H. Yu, S. Chen and H. Zhao, Enhanced photocatalytic performance of a two-dimensional $BiOIO_3$/g-C_3N_4 heterostructured composite with a Z-scheme configuration, *Appl. Catal., B*, 2018, **237**, 947-956.
25. Z. Jin, R. Hu, H. Wang, J. Hu and T. Ren, One-step impregnation method to prepare direct Z-scheme $LaCoO_3$/g-C_3N_4 heterojunction photocatalysts for phenol degradation under visible light, *Appl. Surf. Sci.*, 2019, **491**, 432-442.